processes

MDPI

Article

Evaluation of CO_2/Water Imbibition Relative Permeability Curves in Sandstone Core Flooding—A CFD Study

Tathagata Acharya [1,*], Tapinder Dhaliwal [1], Alina Ludian [2], Gorang Popli [1], Benjamin Wilemon [2], Leonardo Hernandez [2], Maryam Farahani [2] and Liaosha Song [1]

[1] College of Natural Sciences, Mathematics, and Engineering, California State University, Bakersfield, CA 93311, USA; gpopli@csub.edu (G.P.)
[2] Bakersfield College, Bakersfield, CA 93305, USA; alina.ludian5598@email.bakersfieldcollege.edu (A.L.); benjamin.wilemon0000@email.bakersfieldcollege.edu (B.W.); leonardo.hernandez2023@email.bakersfieldcollege.edu (L.H.); maryam.jalalifarahani@bakersfieldcollege.edu (M.F.)
* Correspondence: tacharya@csub.edu

Abstract: Greenhouse gases such as CO_2 can be safely captured and stored in geologic formations, which in turn can reduce the carbon imprint in the Earth's atmosphere and therefore help toward reducing global warming. The relative permeability characteristics in CO_2/brine or CO_2/water systems provide insight into the CO_2 trapping efficacy of formations such as sandstone rocks. In this research, CO_2/water imbibition relative permeability characteristics in a typical sandstone core sample are numerically evaluated. This work uses transient computational fluid dynamics (CFD) simulations to study relative permeability characteristics, and a sensitivity analysis is performed based on two different injection pressures and absolute permeability values of the sandstone rock material. Results show that when the irreducible water fraction remains unchanged, the imbibition relative permeability to the non-wetting phase decreases with an increase in injection pressure within the sandstone core sample. Also, with the irreducible water fraction being unchanged, relative permeabilities to both non-wetting and wetting phases decrease with an increase in the absolute permeability of the rock material. Finally, at irreducible water saturation, relative permeability to the gas phase decreases with an increase in injection pressure.

Keywords: relative permeability; imbibition; computational fluid dynamics

Citation: Acharya, T.; Dhaliwal, T.; Ludian, A.; Popli, G.; Wilemon, B.; Hernandez, L.; Farahani, M.; Song, L. Evaluation of CO_2/Water Imbibition Relative Permeability Curves in Sandstone Core Flooding—A CFD Study. *Processes* **2024**, *12*, 2176. https://doi.org/10.3390/pr12102176

Academic Editor: Federica Raganati

Received: 19 September 2024
Revised: 3 October 2024
Accepted: 5 October 2024
Published: 7 October 2024

1. Introduction

The presence of excessive CO_2 in the atmosphere due to emissions and other anthropogenic causes induces greenhouse effects and poses extreme challenges to the Earth's system. Based on an estimation by The United States Energy Information Administration, in 2019, the country emitted 5130 million metric tons of CO_2 from industries. During the same year, a staggering total of 33,625 million metric tons of CO_2 were emitted worldwide [1]. One potential solution to this problem is geologic carbon capture and sequestration (CCS). The process of geologic carbon sequestration involves capturing CO_2 from industrial facilities, power plants, and the atmosphere. The captured CO_2 is transported and securely stored in deep geologic formations to prevent its release into the atmosphere [2–6].

CO_2 can be stored in geologic formations such as deep saline aquifers through both physical and chemical trapping mechanisms. Using physical trapping mechanisms, CO_2 retains its physical and chemical structure [7,8]. Chemical trapping involves mechanisms such as ionic and mineral trapping resulting in CO_2 changing its physical and chemical structure [9]. The process of physical trapping includes mobile and immobile trapping. When CO_2 is in the pore space and remains at saturations higher than the irreducible saturation, it forms a continuous phase and flows through the formation. While viscous, capillary, and interfacial forces oppose its flow, pressure and buoyancy forces enable it.

During this process, CO_2 continues to migrate upward until it is trapped. On the other hand, immobile trapping of CO_2 occurs when the capillary, viscous, and interfacial forces are larger than pressure and buoyancy forces, and CO_2 exists in its irreducible saturation in pore spaces [9,10]. With the injection of CO_2 into the small pores of rocks naturally containing saline groundwater, the simultaneous process of two or more fluids flowing within the rock pores creates a very complex system. After CO_2 is injected, it continues to move in an upward direction due to the buoyancy forces. While at the leading edge of the plume, CO_2 displaces water or brine through a process called drainage, at its trailing edge, water displaces CO_2 again through a process called imbibition.

The relative permeability of the CO_2/brine or CO_2/water system is an extremely important characteristic that determines the storage efficacy of geologic formations [11–18]. As shown by Equation (1), relative permeability to non-wetting or wetting phases in a two-phase or multiphase system is expressed as the ratio of the effective permeability to the not-wetting or the wetting phase, to the absolute permeability to the wetting phase in single-phase flow [19].

$$k_{ri} = \frac{k_i}{k}, \tag{1}$$

where k_{ri} is the relative permeability of phase 'i', k_i is the effective permeability of phase 'i' in two-phase or multiphase flow, and k is the absolute permeability to the wetting phase.

The effective permeability to a given phase is obtained using Darcy's equation [19]:

$$q_i = -\frac{k_i}{\mu_i} \nabla P_i \tag{2}$$

where ∇P_i is the pressure gradient associated with the phase across the domain of flow, q_i is the flowrate, and μ_i is the dynamic viscosity of the fluid.

Traditionally, the relative permeability measurements are performed through core flooding experiments in the laboratory. The core flooding experiments typically use real rock cores from target brine formations [7]. The drainage experiment involves injecting CO_2 to displace the host fluid, which is either brine or water. On the other hand, during the imbibition experiment, CO_2 is displaced by brine or water.

Until the early 2000s, very few researchers studied relative permeability in CO_2/brine systems. Through this period, much of the focus was on CO_2/oil systems due to the potential usage of CO_2 in enhanced oil recovery systems. The pioneering studies in CO_2/brine systems were performed by Bachu and his research group during the mid-2000–2010s [4,14,15,20–22]. Following this period, many research groups studied CO_2/brine or CO_2/water systems to establish relationships between variables such as relative permeability to the phases, injection pressure or flowrate, porosity, absolute permeability, temperature, and irreducible fractions of water/brine or CO_2 [8,23–28].

Several articles suggested a maximum irreducible CO_2 saturation of approximately 40% when CO_2 saturation varied between 60% and 80% during core-flooding experiments [12,29–32]. Additionally, the relationship between relative permeability and the irreducible non-wetting phase saturation is well established, as it varies with parameters such as rock composition, grain architecture, and fracturing [12].

While most articles discussing relative permeability reported experimental results, numerical studies on core flooding experiments and relative permeability are far too few. Also, many of these articles discussed relative permeability characteristics in oil–water flows [33–38]. Less published literature exists that reports numerical studies on CO_2 versus brine or water relative permeability characteristics. In addition, almost all published numerical studies on CO_2 vs water/brine relative permeability characteristics use pore-scale models [39–42]. For instance, Najafi et al. performed CFD simulations to obtain relative permeability characteristics of CO_2/brine systems at the pore level [39]. Mohammadmoradi and Kantzas used both CFD and DSMC methods to study relative permeability at the pore level, and they revealed that the continuum assumption is strongly dependent on the size of the pores and gas pressure ranges [40]. Presently, CFD data reporting relative

permeability characteristics at the Darcy scale are extremely limited [43–45]. At the Darcy scale, fluid flow through porous media is studied at the macroscopic level, where the porous medium properties are averaged over the volume, which is large enough to contain many pores but small enough to be considered homogeneous [46]. The authors in their previous article reported CFD data on drainage relative permeability characteristics and showed how endpoint relative permeability to the non-wetting phase varied with viscosity ratio [44]. Also, currently, there is no published literature reporting Darcy scale CFD results on CO_2–water imbibition. CFD research in carbon sequestration is cost-effective and yet provides valuable data that otherwise require expensive experimentation. Results obtained using the CFD code can be validated against experimental results in similar conditions.

Finally, for both drainage and imbibition processes, very few published articles exist that discuss how relative permeability to the phases is influenced by injection pressure or flowrate, and absolute permeability. Injection pressure and flowrates are closely related and an increase in injection pressure generally results in an increase in flowrate [47–50]. Among the earliest researchers, Bachu reported that no clear relationships were observed between relative permeability and commonly measured rock characteristics such as porosity and absolute permeability [11]. In addition, although in drainage processes, it is generally accepted that relative permeabilities are independent of flowrates or pressure gradients, published articles reporting similar relationships in CO_2/water imbibition processes are extremely rare. Akin and Demiral performed three-phase relative permeability measurements and suggested that the wetting phase relative permeability curves were more affected than the gas relative permeability curve. In addition, the gas's relative permeability decreased with an increase in flowrate or pressure drop [51]. Tang et al. performed experiments to assess the influence of pressure on the relative permeabilities of the different phases. They reported that the relative permeability of CO_2 was reduced by 57% when the pressure was increased from 12 MPa to 20 MPa [52].

Therefore, it is evident that currently the body of knowledge lacks information about the interrelationships between relative permeabilities to the non-wetting and wetting phases, and commonly measured parameters such as pressure drop across the core, injection flowrate, and the absolute permeability of the rock material. In this research, the authors perform computational fluid dynamics (CFD) simulations to assess the effects of pressure drop and absolute permeability of the rock material on the relative permeabilities to the phases in a CO_2/water system during a typical imbibition experiment.

2. Materials and Methods

In this work, CFD simulations are performed using ANSYS Fluent 18.2 [53]. The authors study imbibition relative permeabilities to the non-wetting phase, CO_2, and the wetting phase, water, as a function of pressure drop across the core and the absolute permeability of the core material. One of the inputs to the code is the porosity of the sandstone core sample, which was measured experimentally on a Vedder sandstone core sample in a co-author's research laboratory. The details of this work are provided in the principal investigator's previous article [44].

2.1. CFD Methodology

The CFD process can be divided into three stages, which are pre-processing, obtaining the solution, and post-processing.

Pre-processing involves creating the geometry and generating the mesh. Before running simulations, the code requires the setting up of physics, selecting the solver, and specifying boundary and initial conditions. The other tasks involved in this step are the selection of the computational algorithm, specification of the discretization method, and setting up of the criteria for convergence.

The final stage of post-processing involves performing analyses on the converged solution and performing comparisons against relevant experimental data. Figure 1 shows a flowchart explaining the CFD methodology [54].

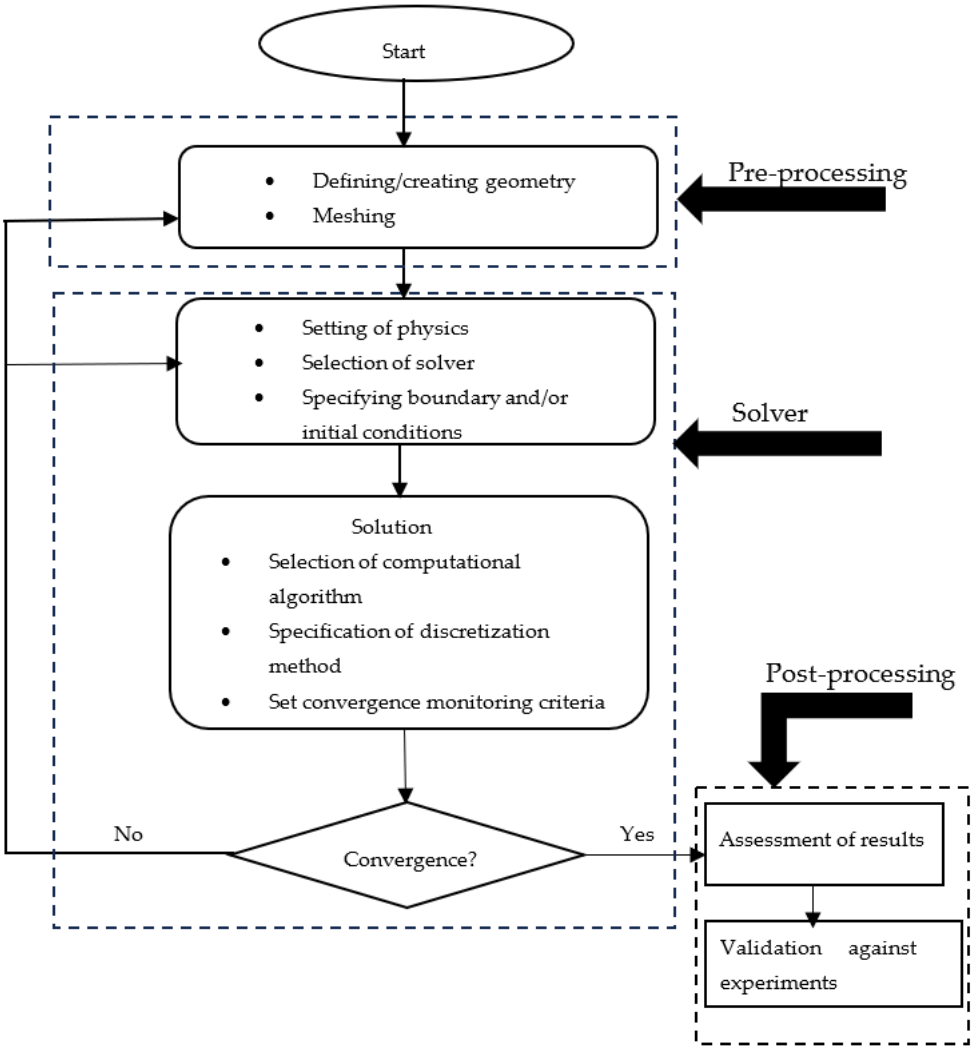

Figure 1. CFD Methodology.

2.2. Simulation Geometry and Meshing

The simulation geometry is a cylindrical sandstone core with a diameter of 38 mm and a length of 79 mm. The mesh elements used are hexahedral in shape and mesh independence is obtained with 1.24 million mesh elements. Figure 2 shows the mesh used in this work.

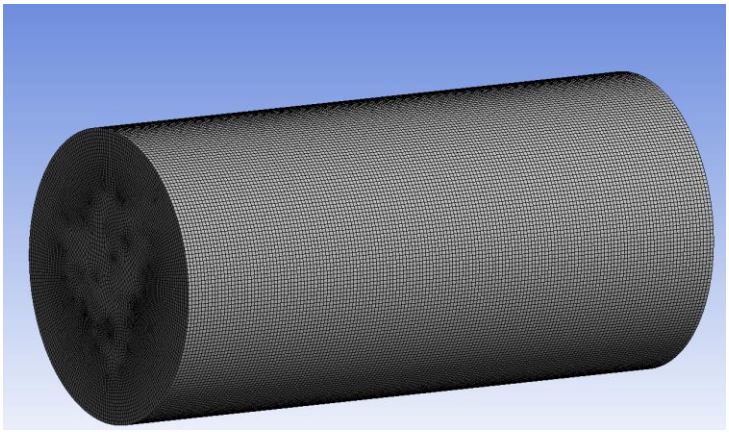

Figure 2. The mesh geometry.

The mesh independence study is conducted by evaluating the water volume fraction 1 s after CO_2 injection during a typical drainage experiment. Figure 3 shows the mesh independence test results.

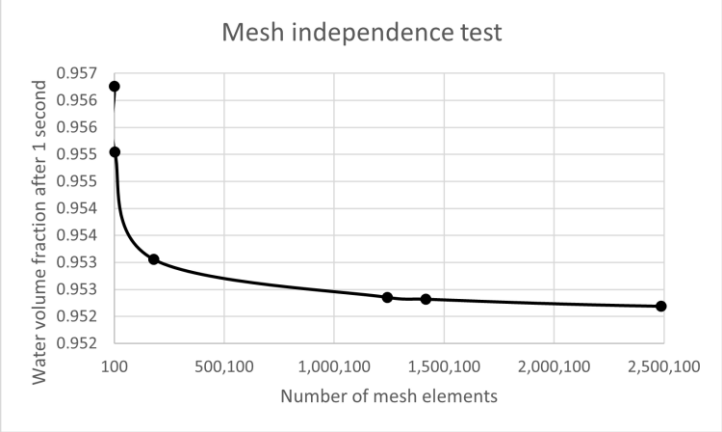

Figure 3. Mesh independence test results [44].

2.3. Model Description and Solver Settings

Transient simulations are performed with the core initially filled with CO_2 during the process of imbibition. The laminar flow model along with the 'Volume of Fluid' (VOF) multiphase flow model is used. The VOF model is useful for tracking the interface between the wetting and non-wetting phases during steady-state or transient simulations. Navier–Stokes equations are solved in three dimensions and the relative permeability to the phases is evaluated every second. Equations (3) and (4) show the mass and momentum conservation equations, respectively [44,52]:

$$\frac{\partial}{\partial t}(\alpha_q \rho_q) + \nabla.\left(\alpha_q \rho_q \vec{v_q}\right) = 0, \tag{3}$$

where α_q is the qth phase volume fraction, ρ_q is the qth phase density, and $\vec{v_q}$ is the qth phase velocity.

The code works by solving a single momentum equation through the domain of flow and both phases share the resulting velocity field [44,53].

$$\frac{\partial}{\partial t}\left(\rho \vec{v}\right) + \nabla.\left(\rho \vec{v}\vec{v}\right) = -\nabla p + \nabla.\left[\mu\left(\nabla \vec{v} + \nabla \vec{v}^T\right)\right] + \rho \vec{g} + \vec{F} \tag{4}$$

where $\vec{g}$ is acceleration due to gravity, p is pressure, and $\vec{F}$ is body force.

The energy equation is only required in non-isothermal flows, and it is used by both phases. It is given by Equation (5).

$$\frac{\partial}{\partial t}(\rho E) + \nabla.\left(\vec{v}(\rho E + p)\right) = \nabla.\left(k_{eff} \nabla T\right) + S_h \tag{5}$$

where k_{eff} is the effective thermal conductivity, E is energy, and T is temperature. The source term S_h includes any contributions from radiation or other heat sources [52]. The porous media within the simulated core sample is modeled using the following terms: (a) viscous resistance, and (b) inertial resistance. The source term that includes the viscous and inertial resistance terms is given by Equation (6):

$$S_i = -\left(\sum_{j=1}^{3} D_{ij} \mu v_j + \sum_{j=1}^{3} C_{ij} \frac{1}{2} \rho |v_j| v_j\right) \tag{6}$$

where C and D are the matrices for inertial and viscous losses, respectively, and S_i is the source term for the i^{th} momentum equation. The model is calibrated by providing empirical values of inertial and viscous resistance coefficients for the targeted absolute permeability of the core sample. In addition, the model also uses the desired value of porosity that is shared by both phases. The model also uses pressure boundary conditions at the inlet and the outlet to replicate the pressure drop across the core. In addition, the model uses an irreducible water fraction of 48.6% as was obtained at the end of the drainage experiment [44]. The convergence criteria for residuals are set as 10^{-5} for all equations. Table 1 shows the boundary and initial conditions used in simulations.

Table 1. Boundary and Initial Conditions.

	Locations	Boundary Type
Boundary Conditions	Inlet	Pressure Inlet
	Outlet	Pressure Outlet
	Body	Wall
Initial Condition	At t = 0, volume fraction of water at inlet = 1	At t = 0, volume fraction of CO_2 in the core other than the inlet = 1

The model used in this research is validated against experimental results reported by previous researchers [45]. The details of this work are provided in the authors' previously published article [44].

2.4. Experimental Conditions

Although permeability generally increases with porosity, it is proportional to the square of pore throat size [55]. Moreover, with the same porosity in two different rock samples, pores may not be equally effective toward facilitating fluid flow. Therefore, it is possible to have rock samples with the same porosity and different permeabilities [56]. For this work, two rock samples having the same dimensions, same porosities, and different permeabilities are simulated. In this study, two identical sandstone core samples with different permeabilities, have a porosity of 18.8%. Also, at both the core inlet and outlet, the temperature is maintained at 50 °C to mimic typical reservoir conditions [57]. At each injection pressure, the absolute permeability values are categorized as high and low based on the classification used by Bachu [11]. The irreducible water saturation at the end of drainage is 48.6% [44].

Table 2 shows the injection pressure and absolute permeability values of the sandstone core samples [11].

Table 2. Injection pressure and absolute permeability to the wetting phase.

Injection Pressure (Pa)	High Absolute Permeability (mD)	Low Absolute Permeability (mD)
400	469	9.89
1000	332	9.56

The dynamic viscosity of CO_2 in the gas phase remains constant during all simulations. Table 3 shows the material properties of fluids used in this work.

Table 3. Material properties of fluid used in the simulations.

Fluid	Density (kg/m^3)	Dynamic Viscosity (Pa.s)
carbon dioxide	1.7878	1.37×10^{-5}
water	998.2	0.001003

3. Results and Discussion

Transient CFD simulations are performed to evaluate the water imbibition process in the sandstone core samples using two different pressure drops across the geometry.

At time t = 0, CO_2 in the gas phase occupies the remaining pore volume of the core while water enters through the inlet.

3.1. High-Permeability Sandstone Core Sample

The absolute permeability to single-phase flow of the wetting phase ranges from 100 mD to 500 mD. Two different injection pressures, 400 Pa and 1000 Pa, are studied.

Figure 4 shows the pressure profile across the high-permeability core, 1 s after start, with an injection pressure of 400 Pa. The core outlet is maintained at atmospheric pressure.

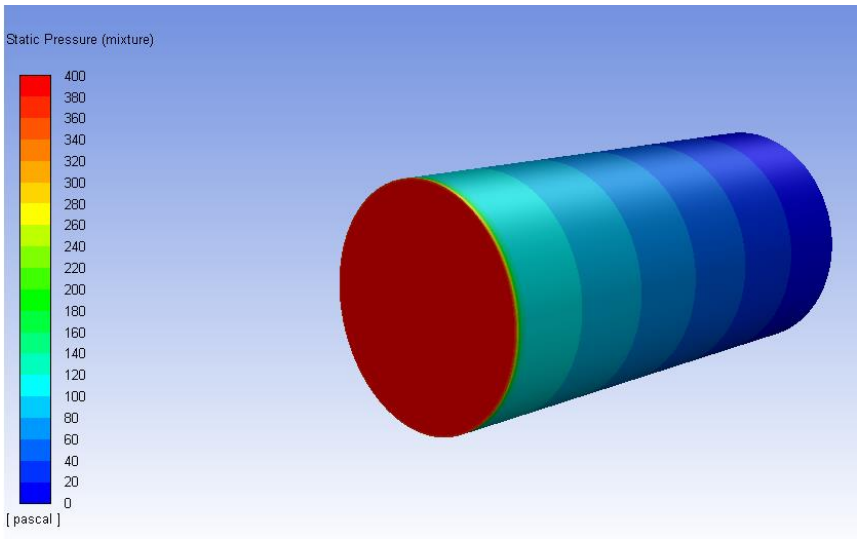

Figure 4. Pressure profile across the high-permeability core 1 s after the start, with Δp = 400 Pa.

Figure 5 shows the pressure profile in the high-permeability core 1 s after the start with an injection pressure of 1000 Pa. While the inlet is set at a gauge pressure of 1000 Pa, the outlet is left open to the atmosphere.

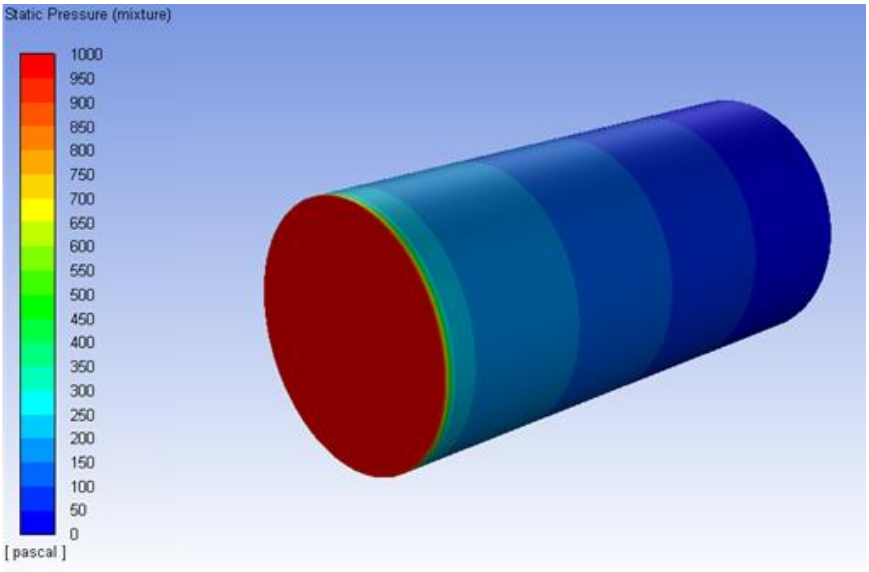

Figure 5. Pressure profile across the high-permeability core 1 s after the start, with Δp = 1000 Pa.

Figure 6 shows the CO_2 volume fraction after 1 s, 60 s, and 240 s with an injection pressure of 400 Pa in the high-permeability core.

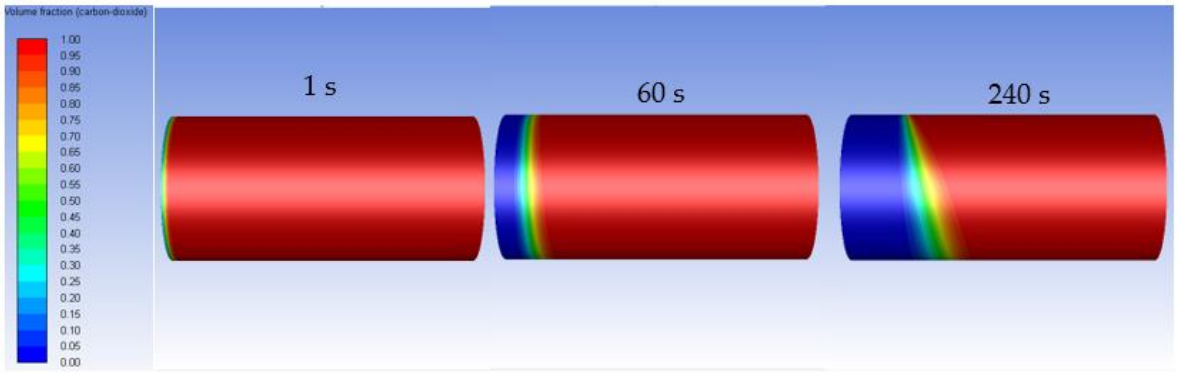

Figure 6. CO_2 volume fraction in the high-permeability core with Δp = 400 Pa.

One second after the start, the volume fraction of CO_2 is nearly one throughout the core, except in the entrance region. The volume fraction of water (the wetting phase) is one at the inlet. After 60 s and 240 s from the start, water displaces CO_2 within the core suggesting imbibition. Figure 7 shows the CO_2 volume fraction after 1 s, 60 s, and 240 s with an injection pressure of 1000 Pa within the high permeability core.

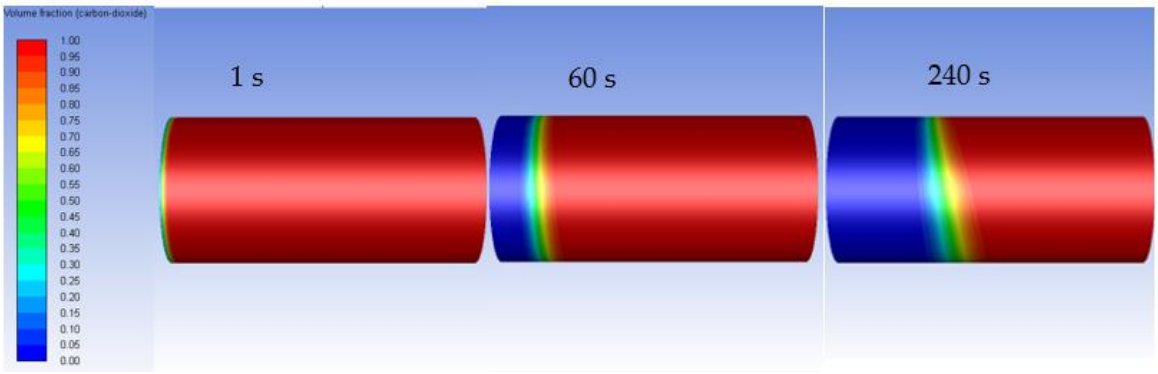

Figure 7. CO_2 volume fraction throughout the high-permeability core with Δp = 1000 Pa.

As expected, a larger injection pressure of 1000 Pa across the core sample results in more water entering the core after 240 s.

3.2. Low-Permeability Sandstone Core Sample

The low-permeability sandstone core, with the same dimensions, is simulated for water imbibition using the same injection pressures of 400 Pa, and 1000 Pa. The absolute permeability to single-phase flow of the wetting phase is less than 10 mD. With the core outlet maintained at atmospheric pressure, Figures 8 and 9 show the pressure profile across the low-permeability sandstone core at injection pressures of 400 Pa and 1000 Pa, respectively.

Figures 10 and 11 show the CO_2 volume fraction after 1s, 60s, and 240s in the low-permeability core with injection pressures of 400 Pa and 1000 Pa, respectively. The results show that less water enters the sandstone core with lower absolute permeability.

Figure 10 shows that, at an injection pressure of 400 Pa, after 240 s, less water enters the low-permeability sandstone core compared to the high-permeability core under the same injection pressure.

Figure 11 shows that, even in the low-permeability core, more water enters the core when the injection pressure is increased from 400 Pa to 1000 Pa.

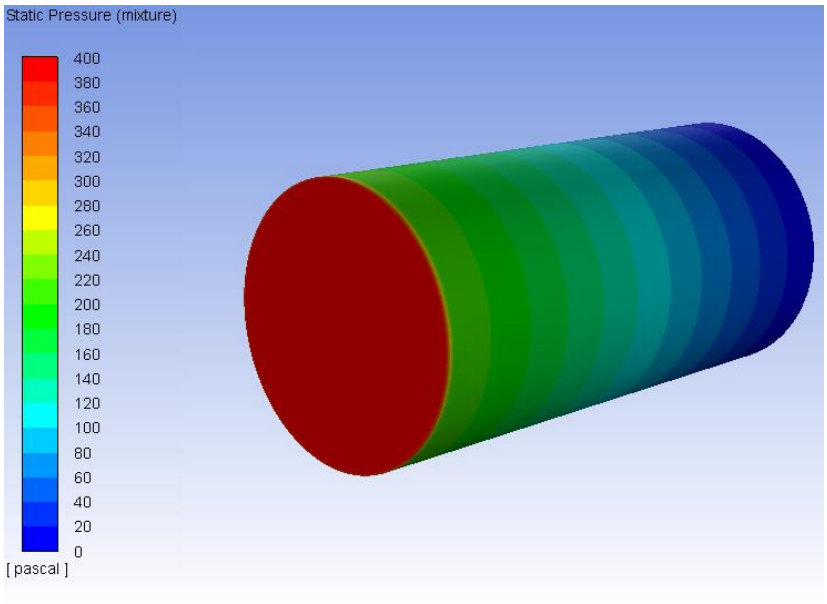

Figure 8. Pressure profile across the low-permeability core 1 s after the start, with Δp = 400 Pa.

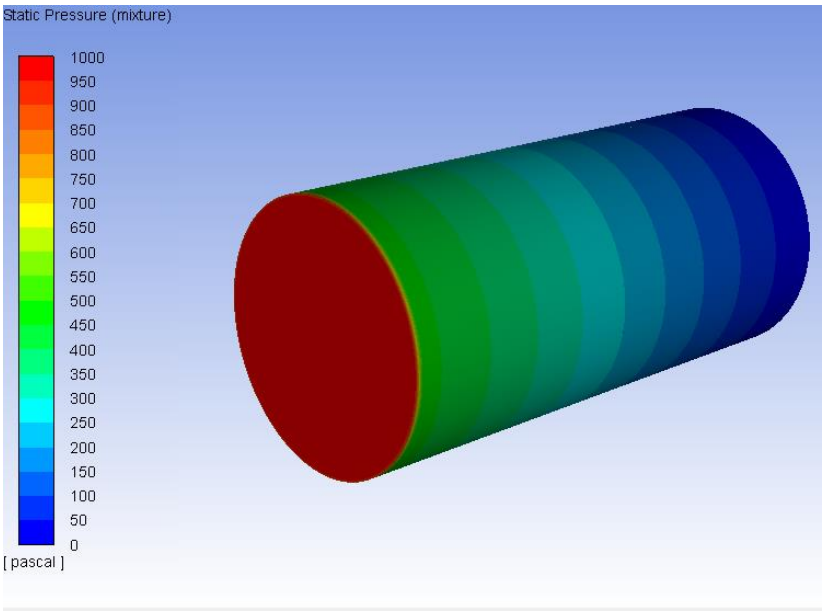

Figure 9. Pressure profile across the low-permeability core 1 s after the start, with Δp = 1000 Pa.

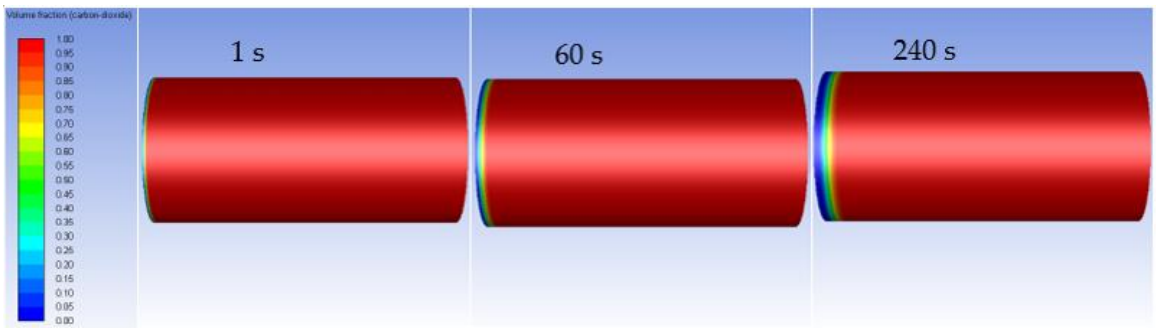

Figure 10. CO_2 volume fraction within the low-permeability core with Δp = 400 Pa.

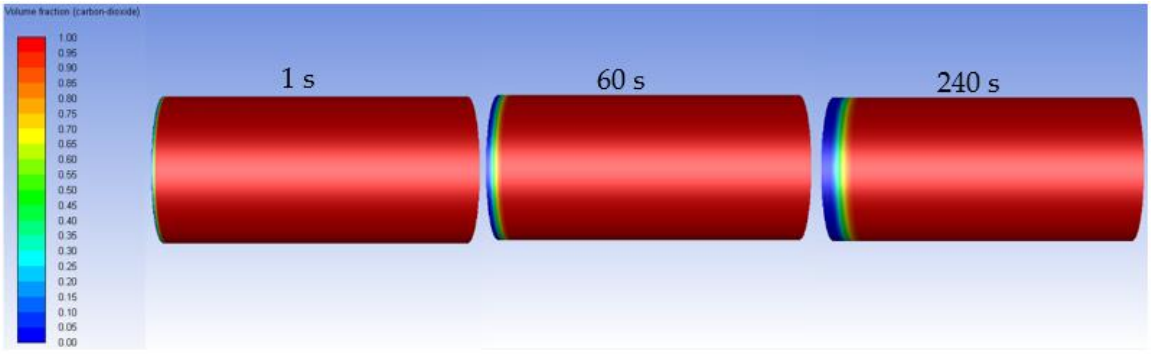

Figure 11. CO_2 volume fraction throughout the low-permeability core with Δp = 1000 Pa.

3.3. Evaluation of Relative Permeability with Varying Injection Pressures for Each Core

Relative permeability curves are obtained as a function of the wetting phase saturation during the process of imbibition. Figure 12 shows the relative permeability curves for the non-wetting and wetting phases with the increase in wetting phase saturation at injection pressures of 400 Pa and 1000 Pa across the high-permeability core.

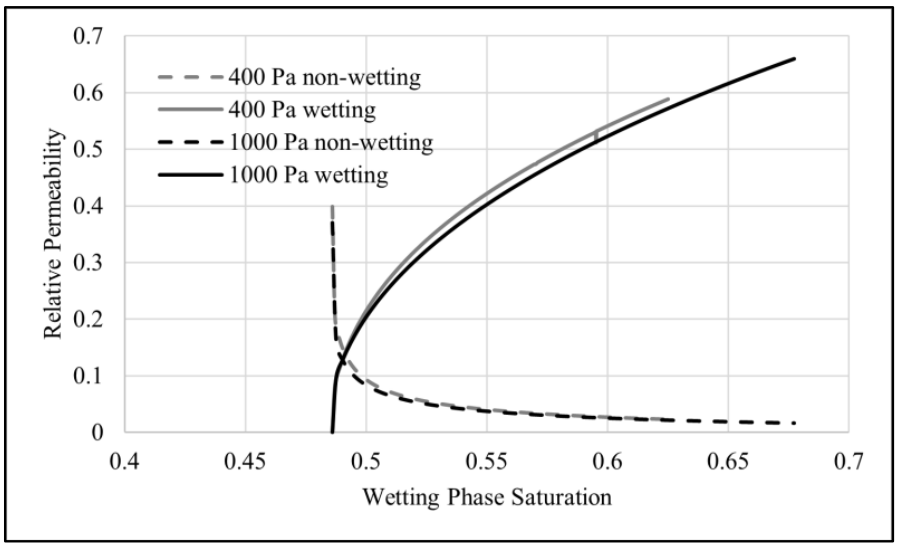

Figure 12. Imbibition relative permeability curves at high absolute permeability.

In the high-permeability sandstone core, the imbibition relative permeability to CO_2 marginally decreases as the pressure drop across the core increases. The relative permeability to water, the wetting phase, also decreases slightly with an increase in injection pressure.

Figure 13 shows the relative permeability curves for both the wetting and non-wetting phases across the low-permeability sandstone core at injection pressures of 400 Pa and 1000 Pa.

While the wetting phase relative permeability is zero at the start of the imbibition process, the non-wetting phase relative permeability slowly tends to zero toward the end of the process. The process is faster in the sample core with high absolute permeability.

Results show that as the injection pressure increases from 400 Pa to 1000 Pa, the relative permeability to both the non-wetting and wetting phases generally decreases.

However, in the high-absolute-permeability core, at wetting phase saturations of 50% or less, the relative permeability to water is marginally higher at 1000 Pa than 400 Pa. As the wetting phase saturation increases, the relative permeability to water at an injection pressure of 1000 Pa gradually becomes lower than at 400 Pa. These observations are also consistent with those in the low-absolute-permeability sandstone core.

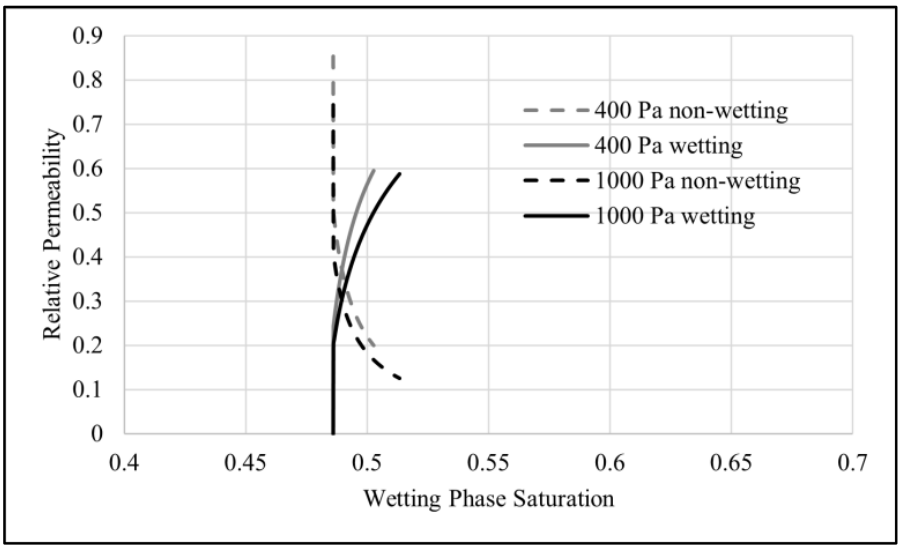

Figure 13. Imbibition relative permeability curves at low absolute permeability.

In both sandstone core samples, the relative permeability to CO_2 or the gas phase decreases as the injection pressure or flowrate increases. This observation agrees with the results reported by previous research groups [51,52]. Also, the relative permeability to CO_2 decreases with an increase in injection pressure at irreducible water saturation. This may be explained by the more pronounced interaction between the phases at higher injection pressures leading to reduced permeability to the gas phase. The decrease in relative permeability to CO_2 with an increase in injection pressure at irreducible water saturation is higher in the low-permeability sandstone core sample.

3.4. Evaluation of Relative Permeability with the Variation in Absolute Permeability at Each Injection Pressure

Figures 14 and 15 show relative permeability to the non-wetting and wetting phases in both high-absolute-permeability and low-absolute-permeability cores at injection pressures of 400 Pa and 1000 Pa, respectively.

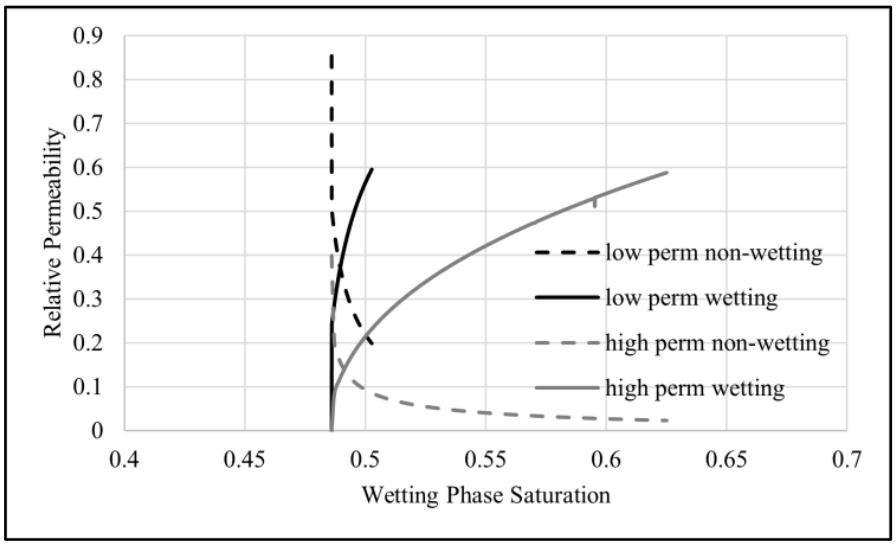

Figure 14. Imbibition relative permeability curves at Δp = 400 Pa.

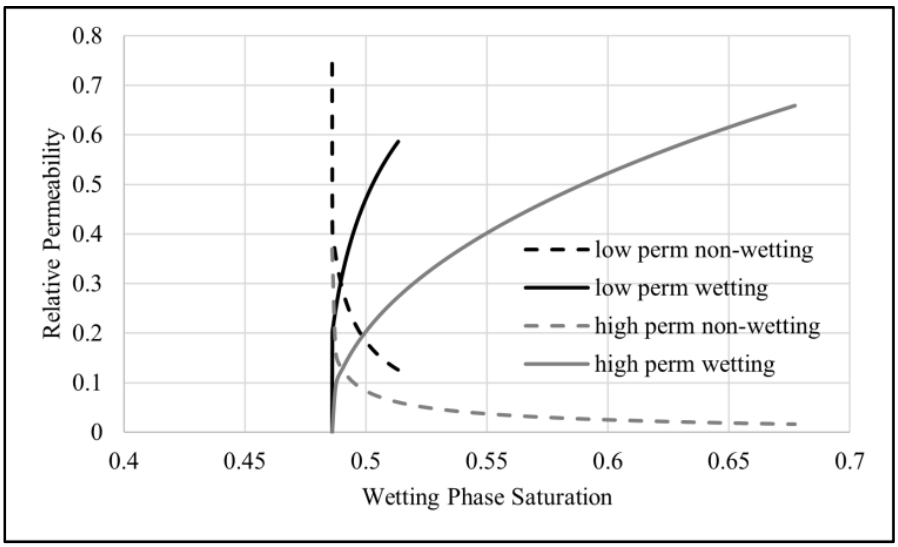

Figure 15. Imbibition relative permeability curves at Δp = 1000 Pa.

With the pressure drop held constant at 400 Pa across the sandstone cores, the relative permeability to both the non-wetting and wetting phases decreases as absolute permeability increases at a given wetting phase saturation level.

Like 400 Pa, at a pressure drop of 1000 Pa, the relative permeabilities to both the non-wetting and wetting phases are lower in the high-absolute-permeability sandstone core at each level of wetting phase saturation.

4. Conclusions

In this study, CFD simulations are used to analyze the imbibition relative permeability characteristics in a CO_2/water system. The study follows the principal investigator's previous article where CFD results on drainage relative permeability curves in an identical sandstone core sample were reported [44]. This work uses data such as the porosity and irreducible water fraction at the end of the drainage experiment from the earlier article. While published literature on CFD results for relative permeability in CO_2/water or CO_2/brine systems is limited, data on how key parameters such as pressure drop, or injection pressure and the absolute permeability of the rock material influence the relative permeabilities are extremely scarce. With little to no published simulation data on Darcy scale core flooding experiments, this is the only article that uses CFD to perform a sensitivity analysis on the influence of injection pressure and absolute permeability on the relative permeability to the phases during imbibition. Simulations are performed by varying the injection pressure in two identical sandstone cores with different values of absolute permeability.

CFD results replicate a typical core flooding imbibition experiment and show that as wetting phase saturation increases, the relative permeability to the wetting phase increases, while the relative permeability to the non-wetting phase decreases. Additionally, as the injection pressure increases from 400 Pa to 1000 Pa, the relative permeability to the gas phase decreases. This effect is more pronounced in the sandstone core sample with lower absolute permeability. These results are consistent with the experimental findings of previous researchers. At irreducible water saturation, the relative permeability to CO_2 reduces with an increase in injection pressure.

Finally, CFD results show that relative permeability characteristics are also affected by the absolute permeability of the rock material when irreducible water saturation, following a drainage experiment, is held constant. The relative permeability to both the non-wetting and wetting phases decreases as the absolute permeability of the rock to the CO_2/water system increases.

Author Contributions: Conceptualization, T.A. and L.S.; methodology, T.A. and M.F.; software, T.A., T.D., G.P., A.L., B.W. and L.H.; validation, T.A.; formal analysis, T.A., T.D., G.P. and A.L.; investigation, T.A. and M.F.; resources, T.A. and L.S.; data curation, T.A. and M.F.; writing—original draft preparation, T.A. and A.L.; writing—review and editing, T.A., A.L., T.D., G.P., B.W., L.H. and M.F.; supervision, T.A.; project administration, T.A., M.F. and L.S.; funding acquisition, T.A. and L.S. All authors have read and agreed to the published version of the manuscript.

Funding: This research was funded through the grant, Chevron California Energy Research Center (CERC) 2024.

Data Availability Statement: Raw data were generated at California State University, Bakersfield. Derived data supporting the findings of this study are available from the corresponding author (T.A.) on request.

Acknowledgments: The authors thank Danielle Carabajal for her technical support on the project.

Conflicts of Interest: The authors declare no conflicts of interest.

References

1. How Much Carbon Dioxide Does the United States and the World Emit Each Year from Energy Resources? Available online: https://www.usgs.gov/faqs/how-much-carbon-dioxide-does-united-states-and-world-emit-each-year-energy-sources (accessed on 4 September 2024).
2. Sun, X.; Shang, A.; Wu, P.; Liu, T.; Li, Y. A review of CO_2 marine geological sequestration. *Processes* **2023**, *11*, 2206. [CrossRef]
3. Al Hameli, F.; Belhaj, H.; Al Dhuhoori, M. CO_2 sequestration overview in geological formations: Trapping mechanisms matrix assessment. *Energies* **2022**, *15*, 7805. [CrossRef]
4. Bachu, S. CO_2 storage in geologic media: Role, means, status and barriers to deployment. *Prog. Energy Combust. Sci.* **2008**, *34*, 254–273. [CrossRef]
5. Holloway, S. Carbon dioxide capture and geological storage. *Philos. Transact. A Math. Phys. Eng. Sci.* **2007**, *365*, 1095–1107. [CrossRef] [PubMed]
6. Orr Jr, F.M. Storage of carbon dioxide in geologic formations. *J. Pet. Technol.* **2004**, *56*, 90–97. [CrossRef]
7. Sun, Y.; Li, Q.; Yang, D.; Liu, X. Laboratory core flooding experimental systems for CO_2 geosequestration: An updated review over the past decade. *J. Rock. Mech. Geotech.* **2016**, *8*, 113–126. [CrossRef]
8. Akbarabadi, M.; Piri, M. Co-sequestration of SO_2 with supercritical CO_2 in carbonates: An experimental study of capillary trapping, relative permeability, and capillary pressure. *Adv. Water. Resour.* **2015**, *77*, 44–56. [CrossRef]
9. Bachu, S. Review of CO_2 storage efficiency and in saline aquifers. *Int. J. Greenhouse Gas Control.* **2015**, *40*, 188–202. [CrossRef]
10. Sadaatpoor, E.; Bryant, S.L.; Sepehrnoori, K. New trapping mechanism in carbon sequestration. *Transp. Porous Media.* **2010**, *82*, 3–17. [CrossRef]
11. Bachu, S. Drainage and imbibition CO_2/brine relative permeability curves at in situ conditions for sandstone formations in western Canada. *Energy Procedia* **2013**, *37*, 4428–4436. [CrossRef]
12. Krevor, S.C.; Pini, R.; Zuo, L.; Benson, S.M. Relative permeability and trapping of CO_2 and water in sandstone rocks at reservoir conditions. *Water Resour. Res.* **2012**, *48*, 1–16. [CrossRef]
13. Busch, A.; Müller, N. Determining CO_2/brine relative permeability and capillary threshold pressures for reservoir rocks and caprocks: Recommendations for development of standard laboratory protocols. *Energy Procedia* **2011**, *4*, 6053–6060. [CrossRef]
14. Bachu, S.; Bennion, B. Effects of in-situ conditions on relative permeability characteristics of CO_2-brine systems. *Environ. Geol.* **2008**, *54*, 1707–1722. [CrossRef]
15. Bennion, D.B.; Bachu, S. Permeability and relative permeability measurements at reservoir conditions for CO_2/water systems in ultralow-permeability confining caprocks. In Proceedings of the SPE Europec featured at EAGE Conference, London, UK, 11 June 2007.
16. Müller, N. Supercritical CO_2/brine relative permeability experiments in reservoir rocks-Literature review and recommendations. *Transp. Porous Media* **2011**, *87*, 367–383. [CrossRef]
17. Farokhpoor, R.; Lindeberg, E.G.B.; Torsaeter, O.; Mørk, M.B.; Mørk, A. Permeability and relative permeability measurements for CO_2-brine system at reservoir conditions in low permeable sandstones in Svalbard. *Greenh. Gases Sci. Technol.* **2014**, *4*, 36–52. [CrossRef]
18. Juanes, R.; Spiteri, E.J.; Orr Jr, F.M.; Blunt, M.J. Impact of relative permeability hysteresis on geological CO_2 storage. *Water Resour. Res.* **2006**, *42*, 1–13. [CrossRef]
19. Fatt, I.; Dykstra, H. Relative permeability studies. *J. Pet. Tech.* **1951**, *3*, 249–256. [CrossRef]
20. Bachu, S.; Bennion, D.B. Experimental assessment of brine and/or CO_2 leakage through well cements at reservoir conditions. *Int. J. Greenhouse Gas Control.* **2009**, *3*, 494–501. [CrossRef]
21. Bachu, S.; Bennion, D.B. Dependence of CO_2-brine interfacial tension on aquifer pressure, temperature and water salinity. *Energy Procedia* **2009**, *1*, 3157–3164. [CrossRef]

22. Bennion, D.B.; Bachu, S. Drainage and imbibition relative permeability relationships for supercritical CO_2/brine and H_2S/brine systems in intergranular sandstone, carbonate, shale, and anhydrite rocks. *SPE Reserv. Eval. Eng.* **2008**, *11*, 487–496. [CrossRef]
23. Deng, H.; Fitts, J.P.; Crandall, D.; McIntyre, D.; Peters, C.A. Alterations of fractures in carbonate rocks by CO_2-acidified brines. *Environ. Sci. Technol.* **2015**, *49*, 10226–10234. [CrossRef] [PubMed]
24. Farokhpoor, R.; Bjørkvik, B.J.; Lindeberg, E.; Torsaeter, O. CO_2 wettability behavior during CO_2 sequestration in saline aquifer-An Experimental study on minerals representing sandstone and carbonate. *Energy Procedia* **2013**, *37*, 5339–5351. [CrossRef]
25. Berg, S.; Oedai, S.; Ott, H. Displacement and mass transfer between saturated and unsaturated CO_2-brine systems in sandstone. *Int. J. Greenhouse Gas Control.* **2013**, *12*, 478–492. [CrossRef]
26. Shi, J.Q.; Xue, Z.; Durucan, S. Supercritical CO_2 core flooding and imbibition in Berea sandstone-CT imaging and numerical simulation. *Energy Procedia.* **2011**, *4*, 5001–5008. [CrossRef]
27. Shi, J.Q.; Xue, Z.; Durucan, S. Supercritical CO_2 core flooding and imbibition in Tako Sandstone-Influence of sub-core scale heterogeneity. *Int. J. Greenhouse Gas Control.* **2011**, *5*, 75–87. [CrossRef]
28. Perrin, J.C.; Benson, S. An experimental study on the influence of sub-core scale heterogeneities on CO_2 distribution in reservoir rocks. *Transp. Porous Media* **2010**, *82*, 93–109. [CrossRef]
29. Ruprecht, C.; Pini, R.; Falta, R.; Benson, S.; Murdoch, L. Hysteretic trapping and relative permeability of CO2 in sandstone at reservoir conditions. *Int. J. Greenhouse Gas Control.* **2014**, *27*, 15–27. [CrossRef]
30. Akbarabadi, M.; Piri, M. Relative permeability hysteresis and capillary trapping characteristics of supercritical CO_2/brine systems: An experimental study at reservoir conditions. *Adv. Water Resour.* **2013**, *52*, 190–206. [CrossRef]
31. Pentland, C.H.; El-Maghraby, R.; Iglauer, S.; Blunt, M.J. Measurements of the capillary trapping of super-critical carbon dioxide in Berea sandstone. *Geophys. Res. Lett.* **2011**, *38*, 1–4. [CrossRef]
32. Pini, R.; Krevor, S.C.; Benson, S.M. Capillary pressure and heterogeneity for the CO2/water system in sandstone rocks at reservoir conditions. *Adv. Water Resour.* **2012**, *38*, 48–59. [CrossRef]
33. Cuevas, J.S.; Gasbarri, S.; Asuaje, M. Computational fluid dynamics for estimating oil-water relative permeability curves. In Proceedings of the SPE Latin America and Caribbean Petroleum Engineering Conference, Maracaibo, Venezuela, 22 May 2014.
34. Iyi, D.; Balogun, Y.; Oyeneyin, B.; Faisal, N. A numerical study of the effects of temperature and injection velocity on oil-water relative permeability for enhanced oil recovery. *Int. J. Heat Mass Transf.* **2022**, *191*, 122863. [CrossRef]
35. Lei, Z.; Liu, T.; Xie, C.; Wang, M.; Zhang, Z. Predictions of relative permeability for low permeability reservoirs and its scale effect. In Proceedings of the SPE Asia Pacific Oil and Gas Conference and Exhibition, Perth, Australia, 25 October 2016.
36. Silva, G.; Correia, B.; Cunha, A.; Santos, B.; Lima, A. Water injection for oil recovery by using reservoir simulation via CFD. *Int. J. Multiphysics.* **2017**, *11*, 83–96.
37. Pinilla, A.; Asuaje, M.; Pantoja, C.; Ramirez, L.; Gomez, J.; Ratkovich, N. CFD study of the water production in mature heavy oil fields with horizontal wells. *PLoS ONE.* **2021**, *16*, e0258870. [CrossRef] [PubMed]
38. Jahan, F.; Hossain, M.M.; Ahmed, S.; Iglauer, S. Investigating impact of various properties on relative permeability and non-wetting phase fractional flow in brine/oil system in water-wet reservoir rock by numerical simulation. In Proceedings of the SPE Western Regional Meeting, Bakersfield, CA, USA, 27 April 2017.
39. Najafi, A.; Siavashi, J.; Ebadi, M.; Orlov, D.; Sharifi, M.; Fahimpour, J.; Moraveji, M.K.; Koroteev, D. Using computational fluid dynamics to compute the pore-scale CO_2-brine relative permeability. *Fuel* **2023**, *341*, 127715. [CrossRef]
40. Mohammadmoradi, P.; Kantzas, A. Pore-scale permeability calculation using CFD and DSMC techniques. In Proceedings of the SPE Rocky Mountain Petroleum Technology Conference/Low-Permeability Reservoirs Symposium, Denver, CO, USA, 5 May 2016.
41. He, D.; Jiang, P.; Lun, Z.; Liu, X.; Xu, R. Pore scale CFD simulation of supercritical carbon dioxide drainage process in porous media saturated with water. *Energ. Source Part A* **2019**, *41*, 1791–1799. [CrossRef]
42. Garimella, S.S.; Ahmed, S.; Hossain, M.M. Comparison of different models for predicting drainage relative permeability using pore scale numerical simulation of supercritical carbon dioxide and brine flow. *IOP Conf. Ser. Mater. Sci. Eng.* **2019**, *495*, 012111. [CrossRef]
43. Papi, A.; Jahanbakhsh, A.; Maroto-Valer, M.M. A new straightforward Darcy-scale compositional solver in OpenFoam for CO_2/water mutual solubility in CO_2 storage processes in aquifers. *Energies* **2024**, *17*, 3401. [CrossRef]
44. Acharya, T.; Song, L.; Duginski, E.; Goodwin, A. Evaluation of relative permeability curves in sandstone core flooding using computational fluid dynamics. *Processes* **2023**, *11*, 780. [CrossRef]
45. Cole, J.; Rasouli, V. Numerical simulations of CO_2 injection into a porous sandstone formation. *WIT Trans. Eng. Sci.* **2012**, *81*, 59–69.
46. Paoli, M.D. Convective mixing in porous media: A review of Darcy, pore-scale and Hele-Shaw studies. *Eur. Phys. J. E* **2023**, *46*, 129. [CrossRef]
47. Jiang, L.; Wang, S.; Li, X.; Liu, J.; Liu, Y.; Xue, Z. The role of flowrates on flow patterns and saturation in high-permeability porous media. *Int. J. Greenh. Gas Control.* **2018**, *78*, 364–374. [CrossRef]
48. Hassani, A.; Mortazavi, S.A.; Gholinezhad, J. A new practical method for determination of critical flowrate in Fahliyan carbonate reservoir. *J. Pet. Sci. Eng.* **2014**, *114*, 50–56. [CrossRef]
49. Rabinovich, A.; Anto-Darkwah, E.; Mishra, A.M. Determining characteristic relative permeability from coreflooding experiments: A simplified model approach. *Water Resour Res.* **2019**, *55*, 8666–8690. [CrossRef]

50. Fakher, S.; Khlaifat, A.L. Experimental investigation of polymer injection in high permeability conduits for material sustainability and behavior in oil reservoirs. *Polymers* **2023**, *15*, 2950. [CrossRef] [PubMed]
51. Akin, S.; Demiral, M.B. Effect of flow rate on imbibition three-phase relative permeabilities and capillary pressures. In Proceedings of the SPE Annual Technical Conference and Exhibition, San Antonio, TX, USA, 5 October 1997.
52. Tang, L.; Ding, G.; Song, S.; Wang, H.; Xie, W.; Zhou, Y.; Song, Z.; Xie, C.; Song, H. Effect of confining pressure in CO_2-brine relative permeability characteristics of sandstone in Ordos Basin. *Water* **2023**, *15*, 4235. [CrossRef]
53. Fluent, ANSYS. *ANSYS Fluent Theory Guide*; ANSYS Inc.: Canonsburg, PA, USA, 2011.
54. Muiruri, P.I.; Motsamai, O.S. Three dimensional CFD simulations of a wind turbine blade section; validation. *J. Eng. Sci. Tech. Rev.* **2018**, *11*, 138–145. [CrossRef]
55. Ma, S.; Morrow, N. Relationships between porosity and permeability for porous rocks. In Proceedings of the International Symposium of the Society of Core Analysts, Montpelier, France, 8–10 September 1996.
56. Bernabé, Y.; Mok, U.; Evans, B. Permeability-porosity relationships in rocks subjected to various evolution processes. *Pure Appl. Geophys.* **2003**, *160*, 937–960. [CrossRef]
57. Wang, Y.; Luce, T.; Ishizawa, C.; Shuck, M.; Smith, K.; Ott, H.; Appel, M. Halitite precipitation and permeability assessment during supercritical CO_2 core flood. In Proceedings of the International Symposium of the Society of Core Analysis, Halifax, NS, Canada, 4–7 October 2010.